**RESEARCH ARTICLE**

**ADVANCED
ENERGY & SUSTAINABILITY
RESEARCH**
Open Access

www.advenergysustres.com

# Strong Electron–Phonon Coupling Induced Self-Trapped Excitons in Double Halide Perovskites

*Baian Chen, Rui Chen,* and Bolong Huang**

Double halide perovskites exhibit impressive potential for the self-trapped exciton (STEs) luminescence. However, the detailed mechanism of the physical nature during the formation process of STEs in double perovskites is still ambiguous. Herein, theoretical research on a series of double halide perovskites $Cs_2B^1B^2Cl_6$ ($B^1 = Na^+$, $K^+$; $B^2 = Al^{3+}$, $Ga^{3+}$, $In^{3+}$) regarding their electronic structures, exciton characteristics, electron–phonon coupling performances, and geometrical configuration is conducted. These materials have flat valence band edges and thus possess localized heavy holes. They also show high exciton binding energies, and their short exciton Bohr radius indicates that the spatial size of their excitons is comparable to the dimension of their single lattice. Based on the Fröhlich coupling constant and Feynman polaron radius, the stronger electron–phonon coupling strength in Ga-series double halide perovskites is revealed. In particular, $Cs_2NaGaCl_6$ shows a high and effective Huang–Rhys factor of 36.21. The phonon characteristics and vibration modes of $Cs_2NaGaCl_6$ are further analyzed, and the Jahn–Teller distortion of the metal–halogen octahedron induced by hole-trapping after excitation is responsible for the existence of STEs. This study strengthens the physical understanding of STEs and provides effective guidance for the design of advanced solid-state phosphors.

B. Chen, B. Huang
Department of Applied Biology and Chemical Technology
The Hong Kong Polytechnic University
Hung Hom, Kowloon, Hong Kong SAR 999077, China
E-mail: bhuang@polyu.edu.hk

B. Chen, R. Chen
Department of Electrical and Electronic Engineering
Southern University of Science and Technology
Shenzhen 518055, China
E-mail: chenr@sustech.edu.cn

B. Huang
Research Centre for Carbon-Strategic Catalysis
The Hong Kong Polytechnic University
Hung Hom, Kowloon, Hong Kong SAR 999077, China

The ORCID identification number(s) for the author(s) of this article can be found under https://doi.org/10.1002/aesr.202300018.

## 1. Introduction

Perovskite materials have attracted significant interests due to their unique properties and broad applications.[1–3] In particular, metal halide perovskites have obtained increasing attention in recent years because of their exceptional properties in the optoelectronic field such as strong light absorption, tunable emission, and low-cost processing.[4–6] These promising materials are potential candidates in wide applications such as optoelectronic sensors, solar cells, and luminous diodes.[7–9] For perovskite photoluminescence, both the narrowband single-color light emission and broadband white light emission have experienced rapid progress in wide aspects.[10–14] Recent observed broadband white-light emissions in halide perovskites, which were attributed to the existence of self-trapped excitons (STEs), show strong significance because of their great potential in solid-state broad photoluminescence.[15–17] In contrast, typical broadband phosphors rely on extrinsic dopants and surface sites.[18,19] The current methods to produce white light can be mixing multiple kinds of phosphors or light-emitting diodes, which can induce inevitable color changes and energy loss.[18] Based on the advanced self-trapping mechanism, halide perovskites can achieve stable and efficient broadband emission to cover the most energy range of visible light, which can further serve as promising single-source emitters.[15] Therefore, these materials are of great potential for broadband photoluminescence and are desirable for the next generation of solid-state phosphors.

Photoluminescence plays an essential role in the optical properties of semiconductors. Exciton luminescence, which belongs to the intrinsic luminescence type,[20] describes the photon-emitting process after the recombination of an exciton. In general, the emission of normal exciton luminescence is mainly determined by the stationary bandgap and exciton-binding energy, so exhibits narrowband photoluminescence. Although narrowband emission builds the importance of exciton materials in many applications such as optical communication.[21] This performance hinders most normal exciton materials from becoming potential solid-state phosphors. The newly found STE emission in halide perovskites features broadband photoluminescence and a large Stokes shift. These promising features are able to create single-source white-light emitters to reduce

the color change and self-absorption effect, which is induced by unequal lifetimes and overlapping absorption ranges of different emitters, respectively.

The formation mechanism of STEs in halide perovskites has been discussed in many studies.[22–28] In general, four factors are considered necessary for the formation of STEs in halide perovskites: intense exciton effect, unique atomic composition as well as the lattice structure, and strong electron–phonon coupling effect. For the exciton effect, Li et al. proposed that the STEs prefer to form in low-dimensional perovskites rather than in bulk materials.[25] This is because, in low-dimensional perovskites, the exciton binding energy inside these materials will be significantly enhanced in the direction perpendicular to the crystal layer because of the strong quantum confinement. This effect improves the existence probability of excitons in low-dimensional perovskites and then increases the corresponding self-trapping density. Other essential issues are the atomic composition and lattice structure of perovskites, which also exhibit the ability to modulate the formation of STEs. For atomic composition, Gautier et al. reported that the self-trapped emission is strong in lead and chloride perovskites but becomes weak in the iodide analog.[26] This indicates that the atomic composition influences the charge distribution as well as the geometric configuration of the lattice, finally affecting the formation of STEs. Moreover, the different arrangements of lattice arrays also have considerable influence on the self-trapping process as reported by Smith et al.[27] The relative intensity of the broadband emission in Pb–Br hybrid perovskites was found to correlate with increasing out-of-plane distortion of the Pb–Br–Pb angle in the inorganic sheets. Especially, the existence of STEs is more reported in double perovskites rather than conventional single perovskites. These newly designed Pb-free metal halide perovskites exhibit outstanding lattice tunability and electronic dimensionalities and provide ample structural possibilities for the formation of STEs. These structural features further lead to another essential factor to influence the nature of self-trapped states in halide perovskites, that is, the electron–phonon coupling effect, which is strictly affected by the atomic composition and lattice structure.[28,29] In detail, electron–phonon coupling describes the process by which the collective excitation of lattice vibration interacts with the motion of a particular electron to change its original wave function. This effect can realize strong interactions between carriers and lattices, which further induce considerable transient lattice defects to trap the primary excitons. This process is further assisted by phonons and identified by investigating the original phonon characteristics of target materials.[20,28] For example, Sui et al. have successfully developed a broadband STE emission (450–600 nm) by building a CdSe superlattice with the strong coupling of excitons and zone-folded longitudinal acoustic phonons.[28]

Indeed, it is possible to realize efficient broadband emission in halide perovskites through an in-depth understanding of STEs and effective material engineering. Therefore, extensive attempts have been made in recent years to further explore the self-trapping nature of halide perovskites. By utilizing the femtosecond transient absorption (FTA) spectroscopy, Wang et al. studied the photophysical properties of different phase halide perovskites and confirmed the key ultrafast trap state capture process in the change of photoluminescence.[30] They have also successfully

analyzed the potential origins of the efficient broadband photoluminescence in halide double perovskites by combining theoretical calculations and FTA experiments.[31,32] In addition, Luo et al. successfully optimized the atomic composition of lead-free halide double perovskites and obtained efficient broadband emissions.[33] However, the atomic contribution of these broadband white lights has not been pointed out directly, which is not conducive to guiding the design of advanced optoelectronic materials with STEs. The exciton effect also needs more discussion to explain its role in the formation process of STEs. The lack of this information hinders further exploration of the intriguing emission features in halide perovskites. Wang et al. discussed the atomic contribution of broadband emission in halide perovskites.[34] Although this study has well explored the origin of broadband emission in halide perovskites, the detailed electron–phonon coupling mechanism of the formation process of STEs still keeps obscure. Therefore, in-depth theoretical evidence and analysis of the formation of STEs need to be further proposed to guide the perovskites engineering for stable and efficient broadband emission.

To bridge the research gap, we aim to examine the excitonic intensity as well as the electron–phonon coupling effect in double halide perovskites to evaluate the self-trapping of excitons by utilizing the first-principle calculation. We first carried out the electronic structures of our six double halide perovskite structures to analyze their basic electronic characteristics. Their energy band diagrams are similar and exhibit some common features: the conduction band minimum (CBM) is gradient, but the valence band maximum (VBM) is flat. This reflects that they have high electron mobility as well as heavy holes. Localized heavy holes will interact with the lattice vibrations and become the prerequisite to be self-trapped. We next calculated the exciton binding energy as well as the exciton Bohr radius of these double halide perovskites by applying the hydrogenic Rydberg model. In general, structures exhibiting high-exciton binding energy and low-exciton Bohr radius are considered to have a significant exciton effect and are selected for further investigation. We then use Fröhlich coupling constants to describe the electron–phonon coupling strength in these structures and calculate their corresponding polaron radii. The energy of self-trapping ($E_{st}$) and lattice deformation ($E_d$), which describe the energy differences of excited and ground states between self-trapping and free configurations, is determined in the configuration coordinate diagrams and is used to estimate the Huang–Rhys factors ($S$) of these lattices. The large Huang–Rhys factor ($S = 36.21$) confirms the strong electron–phonon coupling in double halide perovskite $Cs_2NaGaCl_6$ and the following electron density difference diagram points out the distribution of its STEs. The interaction between electrons and collective lattice vibration causes the $GaCl_6$ octahedron in the excited state to trap a hole, which changes the electronic configuration of $Ga^{3+}$ to $3d^9$. Split energy levels in the crystal field break the spatial symmetry to reduce the degeneracy and cause Jahn–Teller distortion of the $GaCl_6$ octahedron, which is considered as the origin of STEs (**Figure 1**). Our study provided effective analysis as well as methodology in revealing the intrinsic physics of STEs in double halide perovskites, which contributes to guiding further engineering of double halide perovskites in solid-state photoluminescence.
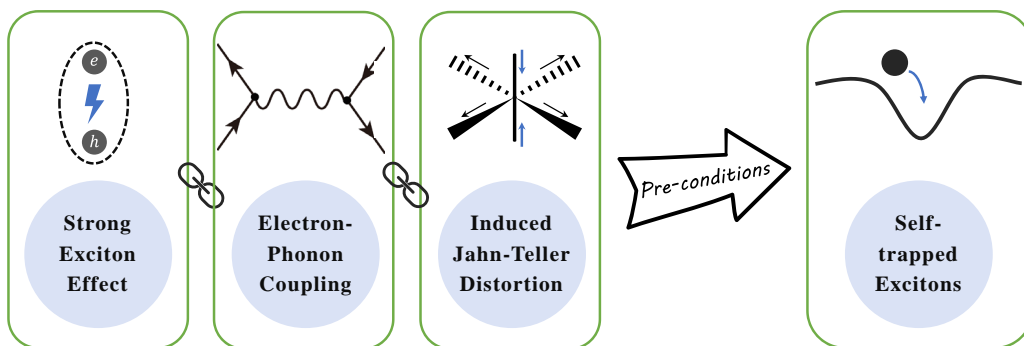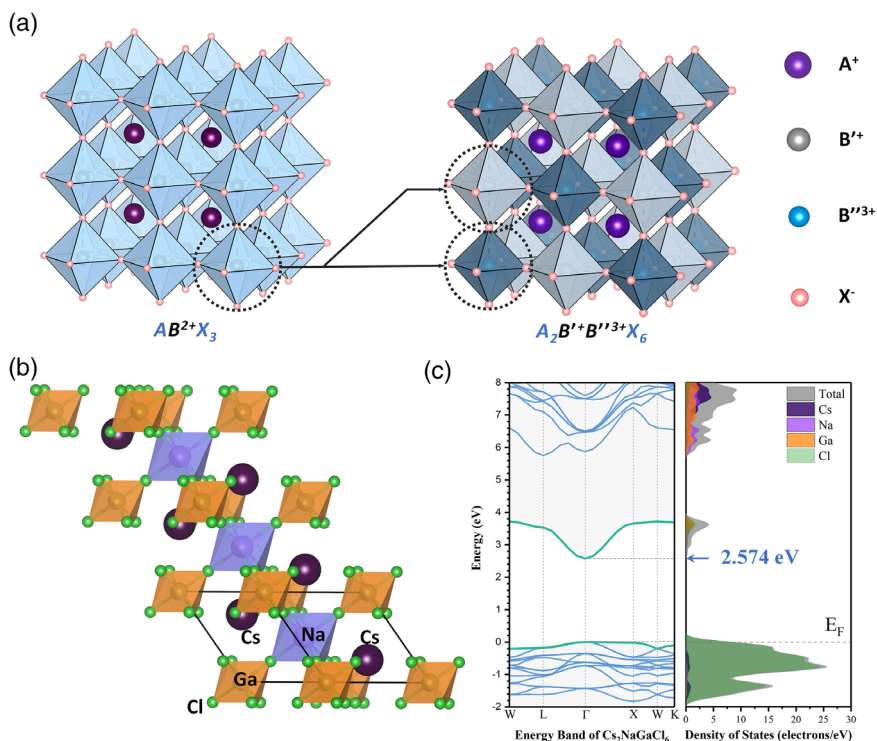
**Figure 1.** Schematic diagram of the preconditions of STE generation.

## 2. Results and Discussions

In this study, we focused on the double halide perovskites $Cs_2B^1B^2Cl_6$ ($B^1 = Na^+$, $K^+$; $B^2 = Al^{3+}$, $Ga^{3+}$, $In^{3+}$) to explore the connections between STEs and their lattice structures. Traditional metal halide perovskites, such as $CsPbCl_3$, show impressive photovoltaic performance due to their high electronic dimensionality and strong antibonding between lead and halogen orbitals.[35–37] However, these emerging materials also suffer serious challenges of their instability at high humidity as well as temperature and toxicity of lead. The combination of trivalent and monovalent cations on the B-sites of traditional metal halide perovskites to form double halide perovskites is an obvious

choice to achieve lead-free lattice and the corresponding structural tunability. Also, as we mentioned above, the enhanced structural tunability of these double halide perovskites can contribute to the formation of STEs to produce broadband emissions. Here, we have chosen the double halide perovskite materials consisting of monovalent ($B^1 = Na^+$, $K^+$) and trivalent cations ($B^2 = Al^{3+}$, $Ga^{3+}$, $In^{3+}$) belonging to the same main group for a brief comparison. Experimentally, some of these materials have been synthesized and exhibited great potential in STEs photoluminescence.[38–40] In this way, we aim to realize the strong STE effect in these materials and achieve an effective exploration of their STE properties with regular atomic compositions. As shown in **Figure 2**a, in our structures, monovalent



**Figure 2.** a) Schematic diagram of atomic composition and lattice structure of double perovskites; b) Lattice structure of the $Cs_2NaGaCl_6$ model. Black lines represent its triclinic lattice and the specified atoms have been labeled; c) Energy band diagram and the density of states of the $Cs_2NaGaCl_6$ model. The gray area represents the total density of states and other colorful areas represent the specified atomic contribution.

($B^1$ = Na$^+$, K$^+$) and trivalent cations ($B^2$ = Al$^{3+}$, Ga$^{3+}$, In$^{3+}$) occupy the original B-sites alternately, forming a corner-sharing 3D array of metal–halogen octahedrons. The optimized lattice structures of our six samples are similar and the representative $Cs_2NaGaCl_6$ lattice structure is shown in Figure 2b. The lattice belongs to the triclinic system and the two different kinds of octahedrons, $NaCl_6$ and $GaCl_6$, are aligned alternately. The basic lattice information of these materials including lattice lengths and bonding angles are presented in Table S1 and S2, Supporting Information. Our calculated bandgap values of these double halide perovskites have shown good consistency with previous works (see Table S3, Supporting Information).

The electronic structure of semiconductors contains key optoelectronic information to elucidate the origin of STEs. We first calculated the electronic structures of these six samples (see Figure S1, Supporting Information) and the energy band diagram of $Cs_2NaGaCl_6$ is shown in Figure 2c. It is worth noting that its CBM exhibits a gradient band edge with broad bandwidth and the band edge of VBM is flat. The gradient conduction band edge reflects the dispersive features as well as the high electron mobility of this material, which contributes to the high electronic dimensionality.[35] In contrast, the flat VBM represents the low mobility of the holes. Through investigating the density of states, it is noted that the valence band edge is mainly contributed by the $GaCl_6$ octahedron. Alternating insertion of $NaCl_6$ octahedrons breaks the orbital continuity of the original 3D $GaCl_6$ octahedral connection networks, resulting in decreased hole mobility. These heavy holes are difficult to diffuse and gradually localized, finally improving the corresponding effective hole mass. The localized holes further interact with surrounding lattices frequently and are easily self-trapped, which is the prerequisite for the formation of STEs.

Strong exciton characteristics also play an important role in the formation process of STEs, which could be well described by exciton binding energy ($E_b$). We next tested the exciton characteristics inside these materials to investigate the STEs features. In general, photogenerated excitons can be regarded as a lone electron–hole pair, and thus its binding energy can be represented by exciton Rydberg energy and estimated by applying the hydrogenic Rydberg model[41]

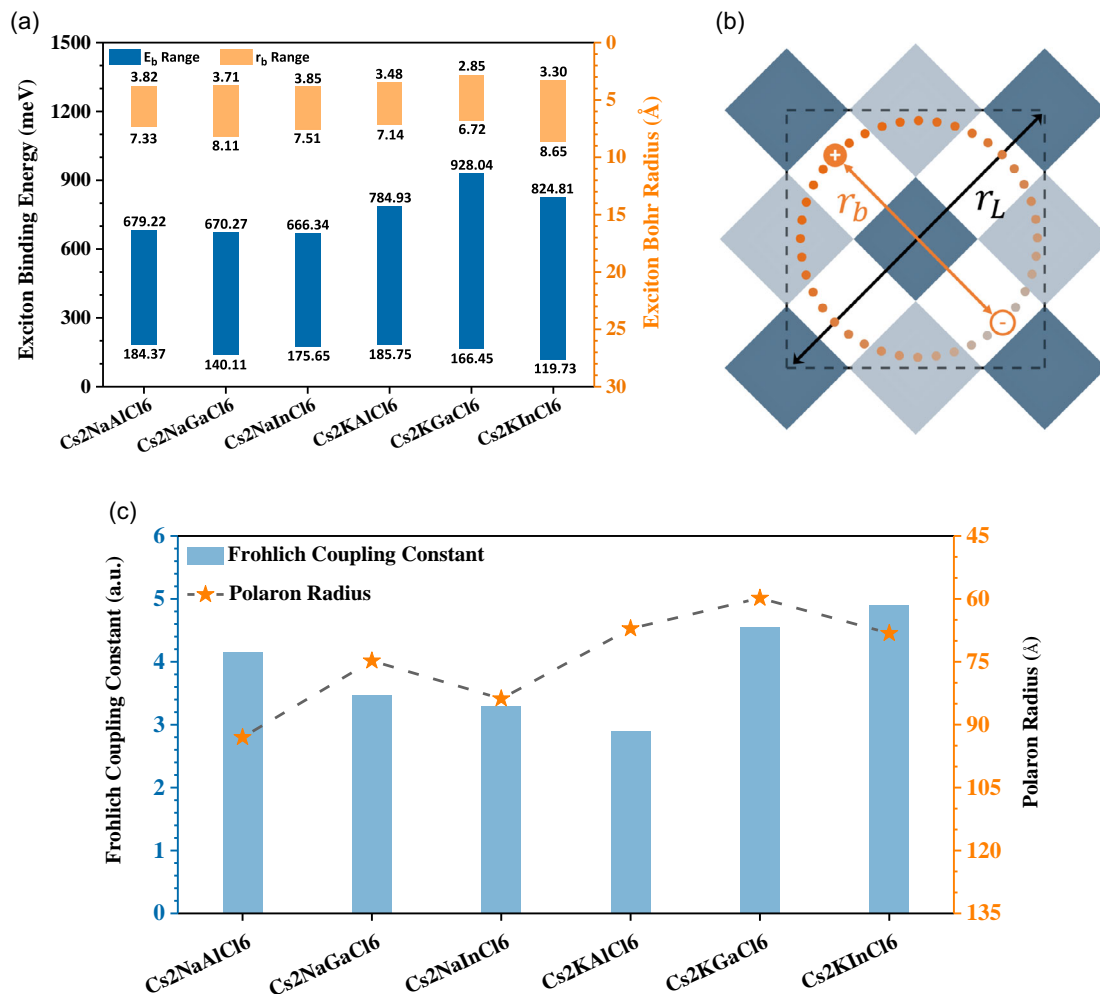$$E_b = \frac{\mu}{m_0 \varepsilon_r^2} R_\gamma \tag{1}$$

where $R_\gamma$ is the Rydberg unit of energy, $\varepsilon_r$ is the relative permittivity, $m_0$ is the electron mass, and $\mu = (m_e^* m_h^*)/(m_e^* + m_h^*)$ represents the reduced mass of the electron–hole pair. Based on the energy band information of these double perovskites, we further obtained the effective masses of electrons ($m_e^*$) and holes ($m_h^*$) at the band edges by calculating $\left(\frac{1}{m^*}\right)_{ij} = \frac{1}{\hbar^2} \frac{\partial^2 E_n(k)}{\partial k_i k_j}$ ($i, j = x, y, z$). The above calculation results of all double halide perovskite are completely presented in **Table 1**. Based on these results, we can identify that the effective mass of holes in these materials is about eight times higher than electrons, consistent with the low hole dimensionality reflected by the valence band edges. As for the permittivity, one issue worth elucidating is that the selection of relative permittivity for the calculation of $E_b$ is still controversial.[42] Frequency-dependent relative permittivity mainly describes the ability of dielectric material to shield the external instantaneous electric field by its internal polarization, which consists of electronic and ionic contributions. The true effective dielectric constant should be a value intermediate between the low-frequency static ($\varepsilon_{static}$) and high-frequency optical ($\varepsilon_\infty$) dielectric constants. In halide perovskites, there is always a large difference between these two dielectric constants, indicating that an arbitrary choice leads to an incomplete result.[42] Therefore, we calculated the upper and lower bounds of $E_b$ and presented the corresponding range of different objects in **Figure 3**a. Another parameter, exciton Bohr radii, which describe the spatial size of the corresponding exciton, can also be calculated by applying formula $r_b = \frac{m_0 \varepsilon_r}{\mu} a_H$. Here, $a_H$ represents the Bohr radius of the hydrogen atom. The range of exciton Bohr radii of these perovskites is also shown in Figure 3b.

As shown in Figure 3a, the lower bound $E_b$ of these perovskites, which is based on the static dielectric constant $\varepsilon_{static}$, is similarly distributed in the range of 100–200 meV. $Cs_2NaAlCl_6$ and $Cs_2KAlCl_6$ have the highest binding energy of ≈185 meV as the lower bound $E_b$ in their corresponding series. Such high values indicate that these double halide perovskite materials have considerable exciton effects compared with the traditional halide perovskites, which have generally larger static dielectric constants ($\varepsilon_{static} \approx 30$) and lower $E_b$ (≈30 meV).[43–45] Meanwhile, the high values of the lower bound $E_b$ of these materials further ensure the basic exciton conditions for the formation of STEs. The upper bound $E_b$ of these double halide perovskites, however, exhibits differences between Na- and K-series materials. Na-series double halide perovskites keep the higher bound $E_b$ of ≈670 meV, while the value of is $Cs_2KGaCl_6$ even more than 900 meV. Compared with Na-series samples, K-series double halide perovskites have higher reduced mass $\mu$ and lower optical dielectric constant $\varepsilon_\infty$ as shown in Table 1, respectively. This suggests that there is a relatively stronger lattice periodic potential field and lower electronic polarization response in these K-series structures and thus, stronger electron-lattice scattering. Interactions between carriers and lattice enhance the quantum confinement of electron–hole pairs after excitation, which is responsible for the higher upper bound $E_b$ of these materials. This judgment also applies to Na-series double halide perovskites above when the comparison objects are traditional halide perovskites. The exciton Bohr radii $r_b$ of these double halide perovskites are also estimated based on the presented data. In general, these values reflect the degree of spatial confinement

**Table 1.** Effective mass of the electron $m_e$, hole $m_h$, and dielectric constants in corresponding double halide perovskites.

| Substance | $m_e(m_0)$ | $m_h(m_0)$ | $\mu(m_0)$ | $\varepsilon_{static}$ | $\varepsilon_\infty$ |
|---|---|---|---|---|---|
| $Cs_2NaAlCl_6$ | 0.44 | 3.10 | 0.39 | 5.33 | 2.78 |
| $Cs_2NaGaCl_6$ | 0.48 | 3.05 | 0.41 | 6.33 | 2.90 |
| $Cs_2NaInCl_6$ | 0.43 | 3.56 | 0.38 | 5.47 | 2.80 |
| $Cs_2KAlCl_6$ | 0.45 | 3.61 | 0.40 | 5.42 | 2.64 |
| $Cs_2KGaCl_6$ | 0.58 | 3.82 | 0.51 | 6.43 | 2.72 |
| $Cs_2KInCl_6$ | 0.48 | 3.68 | 0.43 | 6.95 | 2.65 |

**ADVANCED
SCIENCE NEWS**

www.advancedsciencenews.com

**ADVANCED
ENERGY & SUSTAINABILITY
RESEARCH**
Open Access

www.advenergysustres.com

**Figure 3.** a) Exciton binding energy and Bohr radius range of different double halide perovskites; b) Illustration of exciton situation in double perovskites; The dashed black line represents the side view of one lattice and the orange dashed circle represents an inside exciton. c) Fröhlich coupling constant and polaron radius of different double perovskites.

of electron–hole pairs in crystals and are positively correlated with the exciton effect. It can be seen that the exciton Bohr radius $r_b$ of these double halide perovskites is less than 10 Å in general, which is less than the longest diagonal distance $r_L$ of their triclinic lattices (see Table S2, Supporitng Information). The possible spatial dimensions of excitons in the corresponding lattice of these materials are shown in Figure 3b. Considering the lower bound $r_b$, these materials even possess highly localized excitons of ≈3 Å size inside. This indicates that the excitons of these double halide perovskites are strong Frenkel excitons and are able to trigger significant exciton-lattice coupling to fulfill the prerequisite of the formation of STEs.

After confirming the intense excitonic environment in these double halide perovskites, we further explored the electron-coupling effect. In theory, electrons or holes in ionic crystals polarize their neighbor lattices. Then, the moving carriers can create distortions in lattices and move together as a unified polarization state, which has been called polarons. By assuming that all the essential phonons have the same frequency in the

dielectric crystal lattices, Fröhlich reduced the problem of moving electrons in the lattice potential field to the following Hamiltonian[46]

$$H = \frac{P^2}{2} + \hbar\omega \sum_w b_w^+ b_w + 4\pi i \left(\frac{e^2\hbar}{2\gamma\omega V}\right)^{1/2}$$
$$\sum_w \frac{1}{w}[b_w^+ \exp(-iwr_{el}) - b_w\exp(iwr_{el})] \qquad (2)$$

where $r_{el}$ represents the position vector of the electron and $P$ is the conjugate momentum. $w$ is the momentum, $b_w^+$, $b_w$ represent the corresponding creation and annihilation operators of a phonon, respectively. $V = L^3$ describes the cube volume and $\frac{1}{\gamma} = \frac{\omega^2}{4\pi}\left(\frac{1}{\varepsilon_\infty} - \frac{1}{\varepsilon}\right)$. A dimensionless variable called Fröhlich coupling constant $\alpha$ can hence be extracted from the above equation to describe the electron–lattice interaction strength

**ADVANCED
SCIENCE NEWS**

www.advancedsciencenews.com

**ADVANCED
ENERGY & SUSTAINABILITY
RESEARCH**
Open Access

www.advenergysustres.com

$$\alpha = \frac{1}{4\pi\varepsilon_0}\frac{1}{2}\left(\frac{1}{\varepsilon_\infty} - \frac{1}{\varepsilon_{\text{static}}}\right)\frac{e^2}{\hbar\omega_{\text{LO}}}\left(\frac{2m^*\omega_{\text{LO}}}{\hbar}\right)^{\frac{1}{2}} \tag{3}$$

where $\omega_{\text{LO}}$ represents the characteristic phonon angular frequency of corresponding materials and the dielectric contrast term $\left(\frac{1}{\varepsilon_\infty} - \frac{1}{\varepsilon_{\text{static}}}\right)$ effectively quantifies the carrier–lattice interaction strength in ionic crystals. In our double halide perovskites, there are multiple phonon branches coupled with electrons and so we calculated one effective longitudinal optical phonon frequency by taking a spectral average of all infrared active optical phonon branches[47]

$$\frac{W_e^2}{\Omega_e}\coth(\beta_e/2) = \sum_{i=1}^{m}\frac{W_i^2}{\Omega_i}\coth(\beta_i/2) \tag{4}$$

$$W_e^2 = \sum_{i=1}^{m}W_i^2 \tag{5}$$

$$\beta = \hbar\Omega/k_BT \tag{6}$$

where $\Omega$ is the LO frequencies and $W$ is oscillator strength. To further show the polaron characteristics of these double halide perovskites, we evaluated the corresponding radius and effective mass of polarons for small $\alpha$ by considering the Feynman polaron theory[48,49]

$$r_p = (3/0.44\alpha)^{\frac{1}{2}}(2m_e\omega_{\text{LO}})^{-\frac{1}{2}} \tag{7}$$

$$m_p = 1 + \frac{1}{6}\alpha + \frac{1}{40}\alpha^2 \tag{8}$$

Here, we present the calculation results of the above parameters in **Table 2** and compare the coupling constant $\alpha$ as well as the polaron radius $r_p$ of different double halide perovskites as shown in Figure 3c. These double halide perovskites exhibit considerable Fröhlich coupling constants of $\approx$3–5, which is higher than the average level of traditional halide perovskites ($\approx$2).[50] This indicates that these double halide perovskite structures composed of alternately different metal–halogen octahedron arrangements have a stronger electron–phonon coupling effect. Such a strong electron–phonon coupling effect assists the localized carriers in low electronic dimensionality to interact with the lattice frequently, creating more possibilities for the generation of STEs. In detail, the variation of the coupling constants is related to the collocation degree between $B^1$ and $B^2$ octahedra: smaller $B^2$ octahedron increases the coupling constant in

Na-series double halide perovskites but decreases the coupling constant in K-series ones. Meanwhile, it can be seen that the coupling constant values correlate well with the upper bound $E_b$ of corresponding materials, which are mainly determined by the optical dielectric constant $\varepsilon_\infty$, as mentioned above. This further verifies the interaction between electrons and long-wave polar optical phonons.

The concept of self-trapping originates from the initial sense of polaron, that is, the electron interacting with long-wave polar optic vibrations. When excited electrons keep the inevitable coupling effect with their neighbor lattice vibrations, they can be considered in a self-trapped state, which also applies to excitons.[51] Therefore, polaron properties do counts for the formation process of STEs in crystals. In our study, the polaron radii of these double halide perovskites keep in the range of 60–90 Å. This spatial dimension matches well with 2–3 times the diagonal distance $r_L$ within the lattice. $Cs_2NaGaCl_6$ and $Cs_2KGaCl_6$ own the shortest polaron radius in their corresponding series: 74.46 and 59.80 Å, respectively. Such a short polaron radius reflects the ample influence of lattice vibrations on the mobility of carriers, which induces high effective polaron mass (as shown in Table 2). In addition, the shorter exciton Bohr radius in our materials as mentioned above implies that these polarons, or self-trapped states, are more likely to be caused by Frenkel excitons rather than individual electrons. The distribution of polaron radii of these double halide perovskites, however, is slightly different from the coupling constants after considering the effective mass of electrons $m_e$ and LO frequencies $\omega_{\text{LO}}$. As shown in Figure 2c, the Ga-series double halide perovskites, $Cs_2NaGaCl_6$ and $Cs_2KGaCl_6$, show shorter polaron radii than their analogs, which perform more potential of the existence of STEs.

Since the generation of STEs requires a strong electron–phonon coupling effect, this whole process will definitely lead to the corresponding lattice configuration and energy changes, especially in the excited states. Therefore, we then carried out the configuration coordinate diagrams of these double halide perovskites (Figure S2, Supporting Information) by first computing the coordinate difference as $\Delta Q = \sqrt{\sum_{k,d}M_k(R_{k,d}^E - R_{k,d}^G)^2}$, where $k$, $M$, and $R$ represent the atom, atomic mass, and the position coordinates for excited ($E$) and ground ($G$) states, respectively.[33] $d = (x, y, z)$ denotes different directions. Complete coordinate $Q$ was determined by linear interpolation based on the obtained $\Delta Q$. It can be seen that the optimized excited nuclear configuration has lower potential energy when compared to its primary state and the energy difference is attributed to the self-trapping process ($E_{st}$). Meanwhile, this configuration also increases the potential energy of the original ground state and causes corresponding lattice deformation ($E_d$). In general, the energy component of the whole emission can be regarded as $E_g = E_{st} + E_{PL} + E_d$ and the computed data can be found in Table S4, Supporting Information. The diagrams of $Cs_2NaGaCl_6$ and $Cs_2KGaCl_6$ are presented in **Figure 4**a,b, respectively. Compared to their analogs, $Cs_2NaGaCl_6$ and $Cs_2KGaCl_6$ have obviously higher $E_{st}$ and $E_d$, which match well with their polaron radii characteristics. Smaller polaron radius provides a higher energy barrier for carrier self-trapping and increases $E_{st}$, which contributes to the formation of stable self-trapped states. Meanwhile, the lattice deformation energy $E_d$ is positively
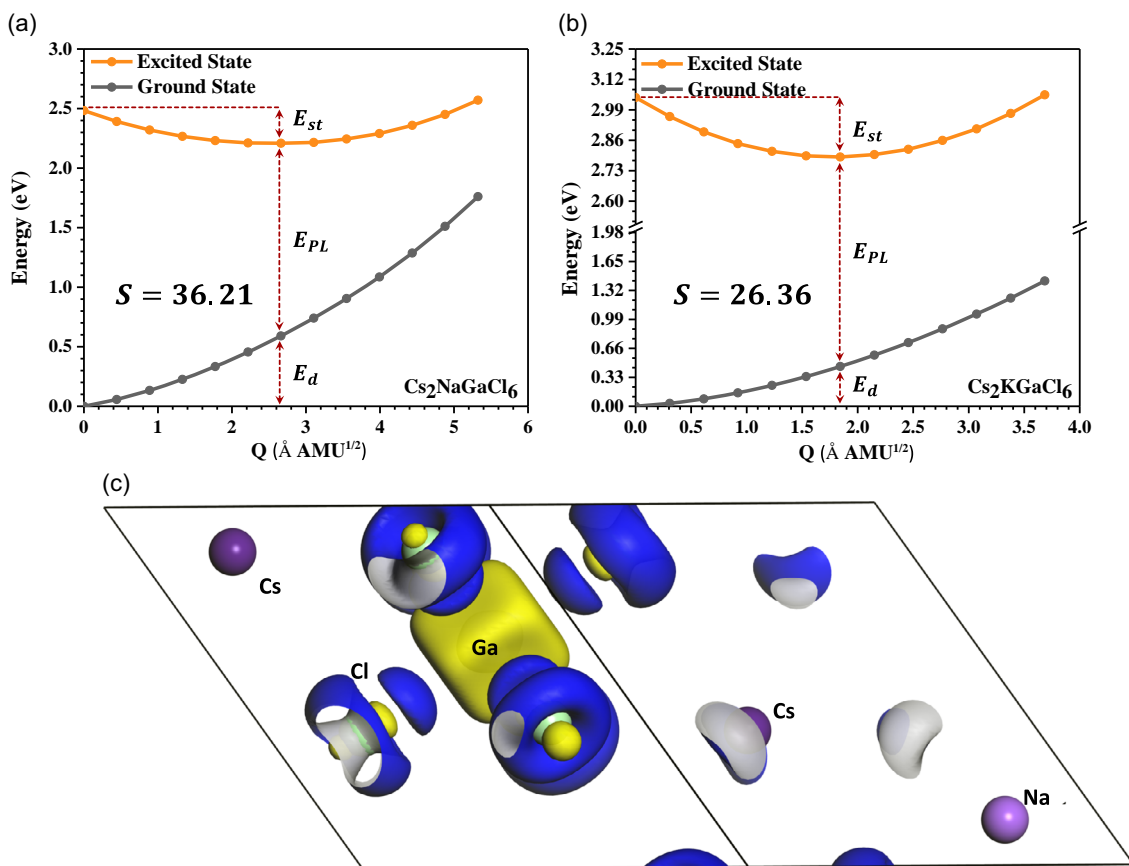
**Table 2.** Effective LO frequencies, coupling constants, and polaron properties of corresponding double halide perovskites.

| Substance | $\omega_{\text{LO}}[\text{cm}^{-1}]$ | $\alpha$ | $r_p(\text{Å})$ | $m_p(m_0)$ |
|---|---|---|---|---|
| $Cs_2NaAlCl_6$ | 83.62 | 4.14 | 93.01 | 0.93 |
| $Cs_2NaGaCl_6$ | 131.61 | 3.74 | 74.76 | 0.94 |
| $Cs_2NaInCl_6$ | 132.45 | 3.28 | 83.80 | 0.78 |
| $Cs_2KAlCl_6$ | 223.22 | 2.90 | 67.08 | 0.77 |
| $Cs_2KGaCl_6$ | 138.89 | 4.54 | 59.80 | 1.33 |
| $Cs_2KInCl_6$ | 120.46 | 4.89 | 68.20 | 1.16 |

**Figure 4.** a) Configuration coordinate diagram of the self-trapping process in $Cs_2NaGaCl_6$ and b) $Cs_2KGaCl_6$. $E_{st}$, $E_{PL}$, and $E_d$ represent the energy of self-trapping, lattice deformation, and photoluminescence, respectively; c) Electron density difference diagram of $Cs_2NaGaCl_6$ describing the self-trapping situation. The blue and yellow areas represent the acquisition of electrons and holes, respectively.

correlated with the self-trapping energy $E_{st}$, where a high $E_d$ value describes a considerable lattice distortion inside these double halide perovskites. This connection implies that the lattice distortion caused by electron–phonon coupling is the exact source of STEs formation.

The Huang–Rhys factor $S = \frac{E_d}{\hbar \Omega_{LO}}$ has been estimated to evaluate the strength of the STE effect in these double halide perovskites.[52] As presented in **Table 3**, all of these structures exhibit a noble electron–phonon coupling effect (see Figure S2, Supporting Information) and $Cs_2NaGaCl_6$ has the highest $S$ value of 36.21, which far exceeds the traditional halide perovskite crystals.[53,54] Meanwhile, the sufficient separation between the curves of the ground and excited state indicates that this high $S$ value does not induce the nonradiative recombination between the electrons and holes in $Cs_2NaGaCl_6$. Therefore, Ga-series double halide perovskites, especially $Cs_2NaGaCl_6$, show potential to be promising candidates for the STEs materials and be further applied in the solid-state photoluminescence field. The electron density difference of excited $Cs_2NaGaCl_6$ after optimization is also visualized in Figure 4c to explore the STEs situation within the lattice. The blue and yellow areas represent the spatial density of electron and hole orbitals, respectively. It is clear that electrons tend to extend toward the vertices of the $GaCl_6$ octahedrons due

**Table 3.** Huang–Rhys factors of different halide perovskites.

| Substance | Huang–Rhys factor $S$ |
| --- | --- |
| $Cs_2NaAlCl_6$ | 16.49 |
| $Cs_2NaGaCl_6$ | 36.21 |
| $Cs_2NaInCl_6$ | 23.38 |
| $Cs_2KAlCl_6$ | 7.19 |
| $Cs_2KGaCl_6$ | 26.36 |
| $Cs_2KInCl_6$ | 17.34 |
| $CsPbBr_3$ (nanosheets) | 3.22[53] |
| $CsPbBr_3$ (microcrystals) | 12.00[54] |

to the strong bonding characteristics and the unique spatial relative position between Ga and Cl atoms. In contrast, the hole orbitals shrink into the center of the $GaCl_6$ octahedrons. This type of geometric confinement, which is consistent well with the large differences of effective mass between electrons and holes as shown in Table 1, will hinder the migration of holes and thus increase the possibility of their self-trapping.

Phonon characteristic is another aspect that needs to be discussed for these structures. In polar semiconductors such

as our double halide perovskite structures, atomic vibrations because of the long-wavelength LO phonons will result in macroscopic polarization and thus an internal electric field, which further enhances the Coulomb interactions between the transferring carriers and crystal lattices.[55] For $Cs_2NaGaCl_6$, there are 10 atoms in one unit lattice, leading to 30 vibration modes in total, including 3 acoustic branches, and 27 optical branches. Its point group is calculated as $O_h$ and the sum symmetry modes at the center of the Brillouin zone can be described with irreducible representations as $\Gamma = 10E_u + 5A_{2u} + 9T_g + 3T_u + 2E_g + A_{1g}$, in which $5E_u + 6T_g + 2T_u + E_g$ are degenerate. Among these vibration modes, $8E_u + 4A_{2u} + 3T_u$ are infrared active modes and $9T_g + 2E_g + A_{1g}$ Raman active modes. Three acoustic modes, $2E_u + A_{2u}$, are silent because of the lack of quadratic functions.[56] We then proposed the diagrams of phonon dispersion curves and phonon state density of $Cs_2NaGaCl_6$ in **Figure 5**a. It can be seen that the LO phonon frequencies are

roughly distributed in three ranges: 40–80 cm$^{-1}$, 100–20, and 220–270 cm$^{-1}$. For the low-frequency LO phonons, Cs atoms contribute the most and the wagging between Cs and Cl atoms becomes the main vibration source. For the higher frequency range 100–200 cm$^{-1}$, which is specified with a pink area as shown in Figure 5a, interactions between Cl and two kinds of metal atoms occupy the most phonon states. The high-frequency stretching between Ga and Cl atoms is responsible for the scarce phonon states in 220–270 cm$^{-1}$. As discussed above, the calculated effective LO frequency of $Cs_2NaGaCl_6$ is 131.61 cm$^{-1}$. Therefore, the main LO phonon branches in this structure, which interact with the moving carriers in the process of electron–phonon coupling, should be closely related to the atomic vibrations between different metal–halogen octahedrons.

To further investigate the exact coupling results between different metal–halogen octahedrons and analyze the origin of STEs, the bond lengths of metal octahedrons in
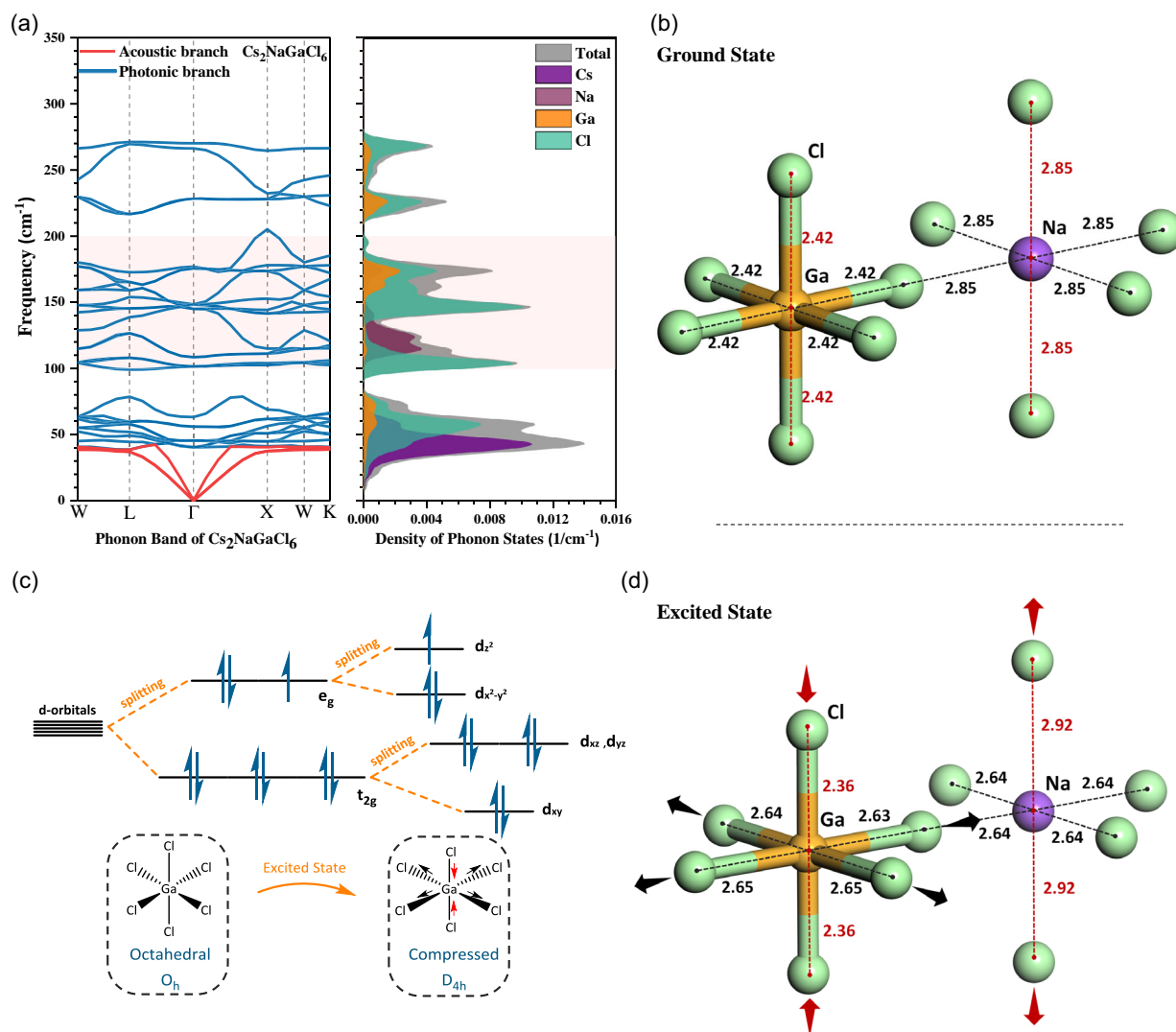


**Figure 5.** a) Phonon dispersion curves and density of phonon states of $Cs_2NaGaCl_6$. The gray area represents the total density of phonon states and other colorful areas represent specified atomic contributions; b) $GaCl_6$ octahedron configuration in the ground state and c) the excited state. The unit of bond length is angstrom (Å); d) Schematic diagram of splitting and occupation of Ga 3d orbitals inducing the Jahn–Teller distortion of $GaCl_6$ octahedron.

**ADVANCED
SCIENCE NEWS**

www.advancedsciencenews.com

**ADVANCED
ENERGY & SUSTAINABILITY
RESEARCH**
Open Access

www.advenergysustres.com

$Cs_2NaGaCl_6$ are compared before and after excitation as shown in Figure 5b,c, respectively. In the ground state, the metal–halogen bond lengths in one octahedron remain uniform, where Ga—Cl bond lengths are 2.42 Å and Na—Cl bond lengths are 2.85 Å. The bonding orbitals between the B-site metal and the halogen atoms tend to achieve the lowest energy stable state, which finally results in the high spatial symmetry of the octahedron system. In contrast, for the excited state, two Cl atoms compact toward the Ga-occupied octahedron center, and the corresponding bond lengths become shorter (2.36 Å), while the remaining four Cl atoms extend away from Ga atoms. In contrast, four bond lengths of the $NaCl_6$ octahedron contract under the influence of the distortion of adjacent $GaCl_6$ octahedrons, while the other two are prolonged. All these distortions indicate the Jahn–Teller effect with the symmetry breaking in solid-state systems.[57] Here, the Jahn–Teller distortions of metal–halogen octahedrons in $Cs_2NaGaCl_6$ couple with the effective LO phonon branches and induce strong carrier–phonon interactions, which is the essential formation origin of STEs.

In the crystal field, the negative electric core formed by the ligand will produce a Coulomb electrostatic effect on the central atom to eliminate the degenerate state of its $d$ orbitals. Considering the $GaCl_6$ octahedron coordination field, this effect will split the original $d$ orbital energy levels of Ga into two sets, $e_g$ and $t_{2g}$, as shown in Figure 5d. For $d_{z^2}$ and $d_{x^2-y^2}$ orbitals, their electron cloud maxima are highly overlapped with the negative coordination field in a head-to-head manner and thus subjected to a large repulsion, which leads to an increase in the orbital energy level. The electron cloud maxima of the other three $d$ orbitals, $d_{xy}$, $d_{xz}$ and $d_{yz}$, are distributed in the crack of the negative coordination field. Therefore, these three $d$ orbitals are more stable and have lower energy levels. Ground state $GaCl_6$ octahedron in $Cs_2NaGaCl_6$ has trivalent Ga ions with normal $3d^{10}$ configuration. Such an electronic configuration causes the formation of a standard regular octahedron with $O_h$ point group by Ga and its surrounding six Cl atoms, which has been confirmed by our discussions. However, the alternating insertion of $NaCl_6$ octahedrons breaks the continuity of orbital overlapping of the original $GaCl_6$ octahedron array, resulting in the localization of holes. These localized holes are mainly distributed in the center of $GaCl_6$ octahedrons and become prone to be self-trapped. After excitation, the self-trapping of one hole changes the electronic configuration of $Ga^{3+}$ to $3d^9$, resulting in the absence of electrons in the $d_{z^2}$ orbital. This then reduces the repulsive force of Ga on the two Cl atoms in ±z orbital directions, causing them to shift inward and form two shorter bonds. The other four Ga-Cl bonds are elongated and as a result, the whole $GaCl_6$ octahedron system is compressed to form a $D_{4h}$ point group. The vibration between two metal–halogen octahedrons then represents the main effective LO phonon branches to couple with the carriers and further strengthen the self-trapping effect. All these processes are driven by a comparable energy stabilization, which can be affected by the degree of excitation because of the hole density. In addition, strong excitonic characteristics further enhance the confinement of these holes by forming stable electron–hole pairs, or excitons, which finally contribute to the high Huang–Rhys factor as well as the formation of STEs in $Cs_2NaGaCl_6$.

## 3. Conclusion

In this work, we applied theoretical calculation to systematically analyze the STEs properties in double halide perovskites $Cs_2B^1B^2Cl_6$ ($B^1 = Na^+, K^+$; $B^2 = Al^{3+}, Ga^{3+}, In^{3+}$). Heavy holes are found in these double halide perovskites and they become prone to be localized and interact with the lattices during the electron–phonon coupling process, which is the prerequisite of the generation of STEs. We then presented the $E_b$ range and our structures exhibit strong excitonic performance with the lower bound $E_b$ in the range of 120–190 meV. The exciton Bohr radii keep in the range of 2–9 Å in general. The intense exciton environment provides sufficient exciton density inside these materials and then increases the potential of STEs generation. In addition, the high Fröhlich coupling constants further confirm the strong interactions between carriers and lattice vibration in these polar crystals. Their nuclear configuration diagrams in the ground and excited state were proposed and the important Huang–Rhys factors were estimated based on the variation of the potential energy surface. $S$ value of $Cs_2NaGaCl_6$ is determined as 36.21 and the STE situation is visualized by the electron density differences diagram. The density of phonon states indicates that the $GaCl_6$ octahedron is strongly coherent with the calculated effective LO phonon frequency in $Cs_2NaGaCl_6$. The differences in bond lengths between the nuclear configurations in the ground and excited states reveal the induced Jahn–Teller distortion of metal–halogen octahedrons. Jahn–Teller distortion in a strong exciton environment, which is assisted by the electron–phonon coupling effect, is confirmed to be the main source of STE generation. Our work contributes to the decoding of the STE formation mechanism and provided theoretical guidance for the design of advanced materials in the solid-state luminescence field.

## Supporting Information

Supporting Information is available from the Wiley Online Library or from the author.

## Conflict of Interest

The authors declare no conflict of interest.

## Data Availability Statement

The data that support the findings of this study are available in the supplementary material of this article.

[1] L. Lu, M. Sun, T. Wu, Q. Lu, B. Chen, B. Huang, *Nanoscale Adv.* **2022**, *4*, 680.

[2] L. Lu, M. Sun, T. Wu, Q. Lu, B. Huang, *Chem. Commun.* **2021**, *57*, 9366.

[3] M. Lu, Y. Zheng, Y. Hu, B. Huang, D. Ji, M. Sun, J. Li, Y. Peng, R. Si, P. Xi, C. H. Yan, *Sci. Adv.* **2022**, *8*, eabq3563.

[4] J. Burschka, N. Pellet, S. J. Moon, R. Humphry Baker, P. Gao, M. K. Nazeeruddin, M. Grätzel, *Nature* **2013**, *499*, 316.

[5] W. Yin, T. Shi, Y. Yan, *Adv. Mater.* **2014**, *26*, 4653.

[6] L. C. Chen, J. C. Chen, C. C. Chen, C. G. Wu, *Nanoscale Res. Lett.* **2015**, *10*, 312.

[7] G. Murtaza, I. Ahmad, B. Amin, A. Afaq, M. Maqbool, J. Maqssod, I. Khan, M. Zahid, *Opt. Mater.* **2011**, *33*, 553.

[8] S. Luo, W. A. Daoud, *J. Mater. Chem. A* **2015**, *3*, 8992.

[9] Z. Ning, X. Gong, R. Comin, G. Walters, F. Fan, O. Voznyy, E. Yassitepe, A. Buin, S. Hoogland, E. H. Sargent, *Nature* **2015**, *523*, 324.

[10] M. Wei, F. P. G. de Arquer, G. Walters, Z. Yang, L. N. Quan, Y. Kim, R. Sabatini, R. Quintero-Bermudez, L. Gao, J. Z. Fan, F. Fan, A. Gold-Parker, M. F. Toney, E. H. Sargent, *Nat. Energy* **2019**, *4*, 197.

[11] A. M. Sanni, S. N. Lavan, Z.-F. Liu, A. S. Rury, *J. Phys. Chem. C* **2021**, *125*, 28004.

[12] S. Bhaumik, A. Bruno, S. Mhaisalkar, *RSC Adv.* **2020**, *10*, 13431.

[13] A. Yangui, S. Pillet, E.-E. Bendeif, A. Lusson, S. Triki, Y. Abid, K. Boukheddaden, *ACS Photonics* **2018**, *5*, 1599.

[14] B. B. Cui, Y. Han, B. Huang, Y. Zhao, X. Wu, L. Liu, G. Cao, Q. Du, N. Liu, W. Zou, M. Sun, L. Wang, X. Liu, J. Wang, H. Zhou, Q. Chen, *Nat. Commun.* **2019**, *10*, 5190.

[15] M. D. Smith, H. I. Karunadasa, *Acc. Chem. Res.* **2018**, *51*, 619.

[16] Z. Zeng, M. Sun, S. Zhang, H. Zhang, X. Shi, S. Ye, B. Huang, Y. Du, C. H. Yan, *Adv. Funct. Mater.* **2022**, *32*, 2204780.

[17] Z. Zeng, B. Huang, X. Wang, L. Lu, Q. Lu, M. Sun, T. Wu, T. Ma, J. Xu, Y. Xu, S. Wang, Y. Du, C. H. Yan, *Adv. Mater.* **2020**, *32*, e2004506.

[18] S. Ye, F. Xiao, Y. X. Pan, Y. Y. Ma, Q. Y. Zhang, *Mater. Sci. Eng.: R: Rep.* **2010**, *71*, 1.

[19] M. J. Bowers, J. R. McBride, S. J. Rosenthal, *J. Am. Chem. Soc.* **2005**, *127*, 15378.

[20] S. Li, J. Luo, J. Liu, J. Tang, *J. Phys. Chem. Lett.* **2019**, *10*, 1999.

[21] Z. Yuan, B. E. Kardynal, R. M. Stevenson, A. J. Shields, C. J. Lobo, K. Cooper, N. S. Beattie, D. A. Ritchie, M. Pepper, *Science* **2002**, *295*, 102.

[22] A. K. S. Song, R. T. Williams, *Self-Trapped Excitons*, 2nd ed., Springer, Berlin **1996**.

[23] S. Ismail-Beigi, S. G. Louie, *Phys. Rev. Lett.* **2005**, *95*, 156401.

[24] Y. Zhang, F. Wang, X. Feng, Z. Zhang, K. Liu, F. Xia, W. Liang, X. Hu, Y. Ma, H. Li, G. Xing, T. Zhai, *Adv. Funct. Mater.* **2022**, *32*, 2205757.

[25] J. Li, H. Wang, D. Li, *Front. Optoelectron.* **2020**, *13*, 225.

[26] R. Gautier, M. Paris, F. Massuyeau, *J. Am. Chem. Soc.* **2019**, *141*, 12619.

[27] M. D. Smith, A. Jaffe, E. R. Dohner, A. M. Lindenberg, H. I. Karunadasa, *Chem. Sci.* **2017**, *8*, 4497.

[28] X. Sui, X. Gao, X. Wu, C. Li, X. Yang, W. Du, Z. Ding, S. Jin, K. Wu, T. C. Sum, P. Gao, J. Liu, X. Wei, J. Zhang, Q. Zhang, Z. Tang, X. Liu, *Nano Lett.* **2021**, *21*, 4137.

[29] B. Wu, W. Ning, Q. Xu, M. Manjappa, M. Feng, S. Ye, J. Fu, S. Lie, T. Yin, F. Wang, T. W. Goh, P. C. Harikesh, Y. K. E. Tay, Z. X. Shen, F. Huang, R. Singh, G. Zhou, F. Gao, T. C. Sum, *Sci. Adv.* **2021**, *7*, eabd3160.

[30] C. Wang, Y. Liu, X. Feng, C. Zhou, Y. Liu, X. Yu, G. Zhao, *Angew. Chem. Int. Ed.* **2019**, *58*, 11642.

[31] C. Wang, M. Sun, H. Wang, G. Zhao, *J. Phys. Chem. Lett.* **2023**, *14*, 164.

[32] C. Wang, Y. Liu, Y. Guo, L. Ma, Y. Liu, C. Zhou, X. Yu, G. Zhao, *Chem. Eng. J.* **2020**, *397*, 125367.

[33] J. Luo, X. Wang, S. Li, J. Liu, Y. Guo, G. Niu, L. Yao, Y. Fu, L. Gao, Q. Dong, C. Zhao, M. Leng, F. Ma, W. Liang, L. Wang, S. Jin, J. Han, L. Zhang, J. Etheridge, J. Wang, Y. Yan, E. H. Sargent, J. Tang, *Nature* **2018**, *563*, 541.

[34] X. Wang, W. Meng, W. Liao, J. Wang, R.-G. Xiong, Y. Yan, *J. Phys. Chem. Lett.* **2019**, *10*, 501.

[35] Z. Xiao, W. Meng, J. Wang, D. B. Mitzi, Y. Yan, *Mater. Horiz.* **2017**, *4*, 206.

[36] W. Yin, J. Yang, J. Kang, Y. Yan, S. Wei, *J. Mater. Chem. A* **2015**, *3*, 8926.

[37] M. Gong, R. Sakidja, R. Goul, D. Ewing, M. Casper, A. Stramel, A. Elliot, J. Z. Wu, *ACS Nano* **2019**, *13*, 1772.

[38] M. B. Gray, S. Hariyani, T. A. Strom, J. D. Majher, J. Brgoch, P. M. Woodward, *J. Mater. Chem. C* **2020**, *8*, 6797.

[39] R. Zeng, L. Zhang, Y. Xue, B. Ke, Z. Zhao, D. Huang, Q. Wei, W. Zhou, B. Zou, *J. Phys. Chem. Lett.* **2020**, *11*, 2053.

[40] A. Noculak, V. Morad, K. M. McCall, S. Yakunin, Y. Shynkarenko, M. Wörle, M. V. Kovalenko, *Chem. Mater.* **2020**, *32*, 5118.

[41] M. Fox, *Optical Properties of Solids*, 2nd ed., Oxford University Press; Oxford New York, New York, **2010**.

[42] M. Baranowski, P. Plochocka, *Adv. Energy Mater.* **2020**, *10*, 1903659.

[43] P. Umari, E. Mosconi, F. De Angelis, *Sci. Rep.* **2014**, *4*, 4467.

[44] F. Brivio, K. T. Butler, A. Walsh, M. van Schilfgaarde, *Phys. Rev. B* **2014**, *89*, 155204.

[45] L. Protesescu, S. Yakunin, M. I. Bodnarchuk, F. Krieg, R. Caputo, C. H. Hendon, R. X. Yang, A. Walsh, M. V. Kovalenko, *Nano Lett.* **2015**, *15*, 3692.

[46] H. Fröhlich, *Adv. Phys.* **1954**, *3*, 325.

[47] R. W. Hellwarth, I. Biaggio, *Phys. Rev. B* **1999**, *60*, 299.

[48] T. D. Schultz, *Phys. Rev.* **1959**, *116*, 526.

[49] R. P. Feynman, *Phys. Rev.* **1955**, *97*, 660.

[50] C. M. Iaru, A. Brodu, N. J. J. van Hoof, S. E. T. ter Huurne, J. Buhot, F. Montanarella, S. Buhbut, P. C. M. Christianen, D. Vanmaekelbergh, C. de Mello Donega, J. G. Rivas, P. M. Koenraad, A. Y. Silov, *Nat. Commun.* **2021**, *12*, 5844.

[51] È. I. Rashba, M. D. Sturge, *Excitons : Selected Chapters*, North-Holland Pub. Co.: Amsterdam, **1987**.

[52] K. Huang, A. Rhys, N. F. Mott, *Proc. R. Soc. London, Ser. A* **1950**, *204*, 406.

[53] X. Lao, Z. Yang, Z. Su, Z. Wang, H. Ye, M. Wang, X. Yao, S. Xu, *Nanoscale* **2018**, *10*, 9949.

[54] F. Pan, J. Li, X. Ma, Y. Nie, B. Liu, H. Ye, *RSC Adv.* **2022**, *12*, 1035.

[55] P. Y. Yu, *Fundamentals of Semiconductors Physics and Materials Properties*, 4th ed., Springer, Berlin; London, **2010**.

[56] B. Chen, M. Sun, R. Chen, B. Huang, *EcoMat* **2022**, *4*, e12201.

[57] M. A. Halcrow, *Chem. Soc. Rev.* **2013**, *42*, 1784.